



HAL
open science

Refined Post-Impact Velocity Prediction for Torque-Controlled Flexible-Joint Robots

Camilo Andres Rey Arias, Wouter Weekers, Marco Morganti, Vincent Padois,
Alessandro Saccon

► **To cite this version:**

Camilo Andres Rey Arias, Wouter Weekers, Marco Morganti, Vincent Padois, Alessandro Saccon. Refined Post-Impact Velocity Prediction for Torque-Controlled Flexible-Joint Robots. IEEE Robotics and Automation Letters, In press. hal-04148817v1

HAL Id: hal-04148817

<https://hal.science/hal-04148817v1>

Submitted on 3 Jul 2023 (v1), last revised 11 Feb 2024 (v3)

HAL is a multi-disciplinary open access archive for the deposit and dissemination of scientific research documents, whether they are published or not. The documents may come from teaching and research institutions in France or abroad, or from public or private research centers.

L'archive ouverte pluridisciplinaire **HAL**, est destinée au dépôt et à la diffusion de documents scientifiques de niveau recherche, publiés ou non, émanant des établissements d'enseignement et de recherche français ou étrangers, des laboratoires publics ou privés.

Refined Post-Impact Velocity Prediction for Torque-Controlled Flexible-Joint Robots

Camilo Andres Rey Arias¹, Wouter Weekers², Marco Morganti¹, Vincent Padois³, Alessandro Saccon²

Abstract—Predicting the post-impact velocity for torque-controlled flexible-joint robots allows the implementation of impact-aware control schemes which exploit intentional collisions for robotic manipulation and locomotion. Starting from the existing rigid-robot post-impact velocity prediction approach [1], this paper shows how an improvement in the prediction quality can be obtained by taking into account impact surface friction, joint motor inertias, gear ratios, and low-level joint torque control gains. Compared to the previous rigid-robot approach, the paper also proposes a more robust method to estimate the gross post-impact velocity profile from experimental data via a polynomial fit, to remove unmodelled and secondary vibratory effects. The approach is illustrated by means of simulation and validated on 50 experimental trials on a commercially available torque-controlled robot. The recorded impact data and prediction algorithms are shared openly for reproducibility.

I. INTRODUCTION

THE work presented here aims to refine a post-impact velocity predictor [1], that enables the use of non-zero velocity contacts for robotic manipulation. Compared to approaches in which contact is established at (near)-zero velocity to minimize impact forces [2], the introduction of non-zero velocity contacts in robotic manipulation enables a reduction in cycle times and energy consumption per cycle, for applications such as pick and place, as well as a higher level of dexterity from which several tasks can profit, e.g., boxing⁴.

For robotic impact-aware manipulation tasks, the implemented control strategies have to account for velocity jumps induced by intended contacts that occur along a trajectory. These jumps, when they are not directly addressed by the control strategy, are seen as a sudden large disturbance in the system which results in poor tracking and might even cause instability. A strategy to compensate for these velocity jumps is reference spreading [3] that has been further developed in [4]–[7], where the focus is on the quality of the reference trajectory. This method prevents unpredictable behaviour which may happen after jumps in the velocity signal due to contacts. The performance of this approach depends on the accuracy of the prediction of the post-impact response.

¹Camilo Andres Rey Arias and Marco Morganti are with Franka Emika GmbH, 80797 Munich, Germany (camiloarac@gmail.com, marco.morganti@franka.de)

²Wouter Weekers and Alessandro Saccon are with the Department of Mechanical Engineering, Eindhoven University of Technology (TU/e), The Netherlands (w.weekers@tue.nl, a.saccon@tue.nl)

³Vincent Padois is with Inria, 33405 Talence, France (vincent.padois@inria.fr)

⁴Refer to Impact-Aware Manipulation <https://i-am-project.eu>

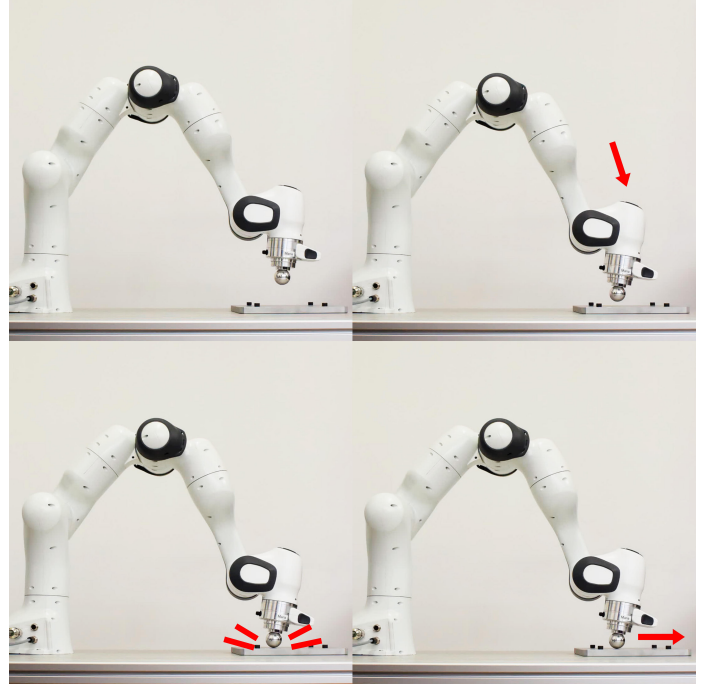


Fig. 1: Illustration of an impact experiment recorded in Franka Emika’s lab with a Franka Emika robot whose end-effector moves downwards and away from the base, before it impacts the steel plate and bounces slightly in the direction displayed by the red arrow in the lower picture on the right. Time evolves from left to right, and from top to bottom.

Proper contact modelling enhances the prediction of the post-impact response. This topic has recently gained relevance in the field of robotic manipulation [1], [8]–[10], as literature focused mainly on impact modelling for locomotion [11], [12] and safe human/robot interactions [13] so far. Furthermore, a large portion of the work in locomotion is based on assuming zero velocity contact [14]–[16], and for non-zero velocity contact there is not much attention given to impact dynamics validation [17], [18]. Therefore, the improvement of the non-zero velocity contact models for robotic manipulators along with subsequent numerical and experimental validation is of high relevance, and that is the goal of this work. Here, the focus is on impacts with a single contact point (as in [1]), leaving the more complex case of impact with multiple simultaneous contact points to future investigation. The recorded impact data [19], the code to compute the prediction and ground truth values of the post-impact velocity using the experimental

data, and the 2D simulation code [20] are openly available for reproducibility.

Impact maps with rigid-body robot models can be used to estimate the post-impact response of flexible joint robots and the accuracy of these predictions can be evaluated quantitatively based on the *quantitative comparison procedure* proposed in [1], although the post-impact response incorporates oscillations that are disregarded by the velocity predictor. The rigid impact map proposed in [1] assumes a frictionless contact between the end-effector and the impacted surface, and it disregards the effects of the low-level joint torque controller. These two modeling decisions reduce the accuracy of the prediction, as shown later in this document. Moreover, the validation of the results is limited to a 2-dimensional scenario (vertical plane). Based on these observations, the main contributions of this work are:

- 1) Analysis of the effects of the modeled motor inertia constant related to the influence of the low-level joint torque controller.
- 2) Introduction of a tangential Coulomb friction term for the contact point.
- 3) Experimental validation with 3D motions.
- 4) Proposal of a more robust alternative fitting method to the post-impact velocity to extract the response without the transients.

The structure of this paper is as follows. Section II presents the dynamics of the system including the low-level joint torque controller, along with the derivation of the refined post-impact velocity predictor. A simulation study for numerical validation of the performance of the predictor is introduced in Section III. Section IV describes the setup for the 3-dimensional experiments conducted to validate the accuracy of the predictor for a 7 degrees-of-freedom (DoF) robot. Finally, the drawn conclusions are stated in Section V.

II. CONTACT MODELING AND DERIVATION OF THE REFINED PREDICTOR

This section presents the flexible-joint robot dynamic model in subsection II-A. The continuous model for the contact between the robot end-effector and the impacted surface is introduced in subsection II-B. Finally, the equivalent rigid-robot model and the proposed impact map are detailed in subsection II-C.

A. Torque-controlled flexible-joint robot dynamics

Consider an n -degrees-of-freedom flexible-joint robot, whose dynamics can be described as (cf., e.g., [21], [22])

$$\boldsymbol{\tau} := \mathbf{K}(\boldsymbol{\theta} - \mathbf{q}), \quad (1)$$

$$\mathbf{M}(\mathbf{q})\ddot{\mathbf{q}} + \mathbf{h}(\mathbf{q}, \dot{\mathbf{q}}) = \boldsymbol{\tau} + \mathbf{D}\mathbf{K}^{-1}\dot{\boldsymbol{\tau}} + \boldsymbol{\tau}_{ext}, \quad (2)$$

$$\mathbf{B}_\rho\ddot{\boldsymbol{\theta}} + \boldsymbol{\tau} + \mathbf{D}\mathbf{K}^{-1}\dot{\boldsymbol{\tau}} = \boldsymbol{\tau}_{act}. \quad (3)$$

Here, $\mathbf{q} \in \mathbb{R}^n$ denotes the link-side joint positions, $\boldsymbol{\theta} \in \mathbb{R}^n$ denotes the motor positions including the gear reduction, $\mathbf{M} \in \mathbb{R}^{n \times n}$ the joint space inertia matrix, $\mathbf{h} \in \mathbb{R}^n$ the Coriolis, centrifugal, and gravity effects, $\mathbf{K} = \text{diag}(k_i) \in \mathbb{R}^{n \times n}$ the joint stiffness matrix, $\mathbf{D} = \text{diag}(d_i) \in \mathbb{R}^{n \times n}$ the joint

damping matrix, $\boldsymbol{\tau}_{ext} \in \mathbb{R}^n$ the externally applied joint torques, $\mathbf{B}_\rho = \text{diag}(b_i) \in \mathbb{R}^{n \times n}$ the motor inertia matrix including the gear reduction, and

$$\boldsymbol{\tau}_{act} = \mathbf{B}_\rho\mathbf{B}_\theta^{-1}\mathbf{u} + (\mathbf{I}_n - \mathbf{B}_\rho\mathbf{B}_\theta^{-1})(\boldsymbol{\tau} + \mathbf{D}\mathbf{K}^{-1}\dot{\boldsymbol{\tau}}) \quad (4a)$$

$$= \mathbf{u} + \mathbf{K}_T(\mathbf{u} - \boldsymbol{\tau}) - \mathbf{K}_S\dot{\boldsymbol{\tau}} \quad (4b)$$

the actuation torques resulting from a low-level control loop, with $\mathbf{K}_T = \text{diag}(k_{T,i}) = \mathbf{B}_\rho\mathbf{B}_\theta^{-1} - \mathbf{I}_n$ a proportional torque gain matrix, $\mathbf{K}_S = \text{diag}(k_{S,i}) = \mathbf{K}_T\mathbf{D}\mathbf{K}^{-1}$ a derivative torque gain matrix, $\mathbf{u} \in \mathbb{R}^n$ the desired link-side torques resulting from a high-level controller, and $\mathbf{B}_\theta = \text{diag}(b_{\theta,i}) \in \mathbb{R}^{n \times n}$ a positive definite matrix such that $b_{\theta,i} < b_i, i = \{1, \dots, n\}$. Note that, by substitution of (4) in (3), the motor-side dynamics is equivalently written as

$$\mathbf{B}_\theta\ddot{\boldsymbol{\theta}} + \boldsymbol{\tau} + \mathbf{D}\mathbf{K}^{-1}\dot{\boldsymbol{\tau}} = \mathbf{u}, \quad (5)$$

showing that the control parameter \mathbf{B}_θ can effectively be considered as a motor inertia matrix whose diagonal entries are reduced compared to those of \mathbf{B}_ρ .

B. Continuous contact model

Given the flexible-joint robot dynamics (1)-(3), the impact dynamics can be incorporated for simulation purposes by adding a continuous contact model (this is an extension of Model A presented in [1] to the case of a robot manipulator). For reasons that will shortly be apparent, the exponentially-extended Hunt-Crossley model [23] is chosen here as the specific continuous contact model. Similar to the conventional Hunt-Crossley model [24] used in [1], the exponentially-extended Hunt-Crossley model prevents non-physical force jumps when establishing contact with nonzero velocity. But, in addition to that, the exponentially-extended Hunt-Crossley model prevents non-physical sticky contact forces to occur upon forced separation at high velocity (an issue the classical Hunt-Crossley model suffers from). Explicitly, the exponentially extended Hunt-Crossley model for fully inelastic impacts reads

$$\mathbf{f}_N = \begin{cases} 0, & \text{if } \delta < 0, \\ k_c\delta^\eta + d_c\delta^\eta\dot{\delta}, & \text{if } \delta \geq 0 \text{ and } \dot{\delta} \geq 0, \\ k_c \exp\left(\frac{d_c}{k_c}\dot{\delta}\right)\delta^\eta & \text{if } \delta \geq 0 \text{ and } \dot{\delta} < 0. \end{cases} \quad (6)$$

In (6), δ is the penetration depth, k_c is the nonlinear stiffness, d_c is the damping factor, and η is Hertz' geometry-dependent contact parameter. Given the expression for f_N in (6), the contact and impact effects can be added to (2) by setting $\boldsymbol{\tau}_{ext} = \mathbf{J}_N(\mathbf{q})^\top \mathbf{f}_N$, where $\mathbf{J}_N(\mathbf{q})$ is the row of the contact Jacobian associated with the linear velocity in the contact normal direction. Tangential contact forces could also be added, but are not discussed here for the sake of brevity.

C. Equivalent rigid-robot model and rigid impact map

To obtain a description of the rigid-joint robot dynamics based on the flexible-joint robot dynamics to be used to predict the post-impact response via a rigid impact map (denoted as

Model C in [1]), τ can be substituted in (2) by its expression as a function of \mathbf{u} , $\dot{\tau}$, and $\ddot{\theta}$ in (5) to obtain

$$\mathbf{M}(\mathbf{q})\ddot{\mathbf{q}} + \mathbf{h}(\mathbf{q}, \dot{\mathbf{q}}) = \mathbf{u} - \mathbf{B}_\theta \ddot{\theta} + \tau_{ext}. \quad (7)$$

The above relationship is valid for any value of joint stiffness \mathbf{K} . Therefore, assuming that the limit of the dynamics for $\mathbf{K} \rightarrow \infty$ would exist, also implying that $\ddot{\mathbf{q}} \equiv \ddot{\theta}$, then one would obtain

$$(\mathbf{M}(\mathbf{q}) + \mathbf{B}_\theta) \ddot{\mathbf{q}} + \mathbf{h}(\mathbf{q}, \dot{\mathbf{q}}) = \mathbf{u} + \tau_{ext}. \quad (8)$$

Equation (8), that we call *the rigid-joint robot model associated with the torque-controlled flexible-joint robot model* (1)-(4), has a mass matrix which is corrected by the apparent motor inertia \mathbf{B}_θ , that in turn depends on the actual motor inertia \mathbf{B}_ρ and the low-level torque control gain \mathbf{K}_T . Equation (8) has already appeared in [25] in the context of singular perturbation analysis of the torque-controlled flexible-joint robot dynamics (1)-(4). The observation that the mass matrix is corrected by the apparent motor inertia is important for the results discussed in Sections III and IV. However, it is important to recall that the rigid-joint robot model is derived under the assumptions that 1) the low-level control loop (4) reduces the motor dynamics (3) to (5), and 2) the motor-side joint accelerations $\ddot{\theta}$ are equivalent to the link-side joint accelerations $\ddot{\mathbf{q}}$. The validity of these assumptions especially under hard impacts is unclear, due to the short time scale typically associated with impacts (typically a few milliseconds) and the finite bandwidth of the low-level control loop. Therefore, in Sections III and IV, extensive numerical and experimental validation is performed to assess the ability of the rigid-robot model (8) to capture the gross velocity jump of the model (1)-(4) after an impact, without explicitly modeling the flexible joint dynamics. The rest of this subsection is devoted to the derivation of the impact map corresponding to the rigid-joint robot model expressed by (8). To this end we start with the following impact-equation

$$\mathbf{M}_\theta(\dot{\mathbf{q}}^+ - \dot{\mathbf{q}}^-) = \mathbf{J}_N^\top \boldsymbol{\Lambda}_N + \mathbf{J}_T^\top \boldsymbol{\Lambda}_T, \quad (9)$$

where $\mathbf{M}_\theta = \mathbf{M}(\mathbf{q}) + \mathbf{B}_\theta$, $\boldsymbol{\Lambda}_N$ and $\boldsymbol{\Lambda}_T$ represent the normal and tangential impulsive forces, $\dot{\mathbf{q}}^+ \in \mathbb{R}^n$ the post-impact joint velocity, $\dot{\mathbf{q}}^- \in \mathbb{R}^n$ the ante-impact joint velocity.

Equation (9) can be simplified using the definition of the frictional force

$$\boldsymbol{\Lambda}_T = -\mu \mathbf{u}_T \boldsymbol{\Lambda}_N, \quad (10)$$

with μ the friction coefficient and \mathbf{u}_T the normalized 2-dimensional direction of the frictional force determined using the ante-impact cartesian velocity along the xy -plane, \mathbf{v}_{xy}^- , as

$$\mathbf{u}_T = \frac{\mathbf{v}_{xy}^-}{\|\mathbf{v}_{xy}^-\|}. \quad (11)$$

Substituting (10) into (9), we obtain

$$\mathbf{M}_\theta(\dot{\mathbf{q}}^+ - \dot{\mathbf{q}}^-) = (\mathbf{J}_N^\top - \mu \mathbf{J}_T^\top \mathbf{u}_T) \boldsymbol{\Lambda}_N, \quad (12)$$

or equivalently

$$\dot{\mathbf{q}}^+ = \dot{\mathbf{q}}^- + \mathbf{M}_\theta^{-1} \tilde{\mathbf{J}}_\mu^\top \boldsymbol{\Lambda}_N, \quad (13)$$

where $\tilde{\mathbf{J}}_\mu$ is defined as $\mathbf{J}_N - \mu \mathbf{u}_T^\top \mathbf{J}_T$.

Considering a perfectly inelastic impact law in the Cartesian space

$$\mathbf{J}_N \dot{\mathbf{q}}^+ = 0, \quad (14)$$

and substituting (13) into (14), we get

$$\boldsymbol{\Lambda}_N = -(\mathbf{J}_N \mathbf{M}_\theta^{-1} \tilde{\mathbf{J}}_\mu^\top)^{-1} \mathbf{J}_N \dot{\mathbf{q}}^-. \quad (15)$$

Finally, substituting (15) into (13) leads to the post-impact velocity predictor

$$\dot{\mathbf{q}}^+ = \left[\mathbf{I}_7 - \mathbf{M}_\theta^{-1} \tilde{\mathbf{J}}_\mu^\top (\mathbf{J}_N \mathbf{M}_\theta^{-1} \tilde{\mathbf{J}}_\mu^\top)^{-1} \mathbf{J}_N \right] \dot{\mathbf{q}}^-. \quad (16)$$

Compared to the original expression for the post-impact velocity predictor in [1, Equation 5], (16) contains two additional effects: first, the explicit dependence on \mathbf{K}_T and \mathbf{B}_ρ appearing via the mass matrix \mathbf{M}_θ ; second, the effect of tangential friction via the coefficient μ . These two factors were not included in [1].

III. RIGID-ROBOT MODEL VALIDATION

This section is devoted to present numerical evidence that the rigid-robot model (8) associated with the flexible-joint robot with joint-torque control (1)-(4) is able to accurately predict the gross velocity jump after an impact. More precisely, the post-impact velocity prediction is obtained by employing the rigid-robot impact map (16) with $\mu = 0$, derived by following the standard procedure of nonsmooth mechanics to combine the impact equation (9) with tangential and normal impact laws (10)-(11) and (14).

In this simulation study we consider a planar RRR-manipulator, based on joints 2, 4, and 6 of the Franka Emika Robot. We use a task-based QP controller with a sample rate of 1 kHz to generate the desired joint torques \mathbf{u} needed to follow a linear trajectory from an initial point to a point below the contact surface, to impact the surface with a desired impact velocity and approach angle. The low-level control-loop (4), which is implemented with a sample rate of 4 kHz (mimicking the robot's internal low-level torque controller), uses the desired joint torques \mathbf{u} to compute the real actuation torques based on the motor accelerations and the measured joint torques. The torque measurements are filtered with a first-order low-pass filter with a cut-off frequency of 300 Hz in order to include the delay effect that the sensors add on the real robot. The link lengths l_i , masses m_i , rotational inertias I_i , and center of mass positions $(c_{x,i}, c_{y,i})$, are determined by lumping the corresponding parameters of the Franka Emika Robot's second and third, fourth and fifth, and sixth, seventh and end-effector link, identified in [26]. The resulting parameters, along with several others used in the simulations⁵, are summarized in Table I.

The simulations clearly support the claim that the rigid-joint robot model (8) with the impact map (16) is capable of capturing the main post-impact response of a flexible-joint robot, as long as the right inertia matrix $\mathbf{M}_\theta = \mathbf{M} + \mathbf{B}_\theta$ is used. More in detail, the following two key observations can

⁵The simulation scripts are available via <https://gitlab.tue.nl/robotics-lab-public/refined-post-impact-velocity-prediction>.

TABLE I: Planar RRR-robot simulation parameters

Link/Joint number →	1	2	3	Units ↓
m_i	3.8755	4.8138	2.7481	[kg]
I_i	0.0977	0.3804	0.0490	[kg·m ²]
$c_{x,i}$	-0.1152	-0.2173	-0.0928	[m]
$c_{y,i}$	0.0320	0.0274	0.0408	[m]
l_i	0.327	0.393	0.167	[m]
d_i	15	15	10	[Nm·s/rad]
k_i	15·10 ³	15·10 ³	10·10 ³	[Nm/rad]
b_i	0.6	0.45	0.2	[kg·m ²]
$b_{\theta,i}$	0.15	0.1125	0.05	[kg·m ²]
η		1.5		[-]
k_c		3.2·10 ⁹		[N/m ^{η}]
d_c		3.2·10 ¹²		[N·s/m ^{$\eta+1$}]

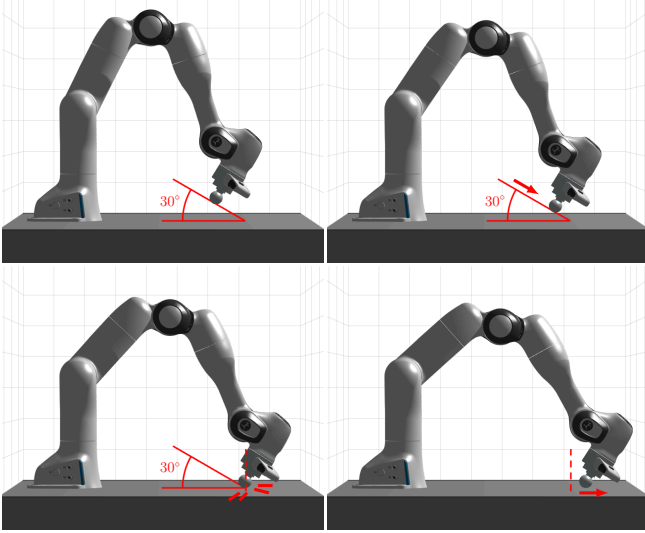


Fig. 2: Visualization of a simulated impact scenario with an approach angle of 30 degrees and an impact velocity of 0.1 m/s. Time evolves from left to right, and from top to bottom. The impact location is indicated by the vertical dashed line.

be made. First, the magnitude of the velocity jump observed for the rigid-robot model associated to the torque-controlled flexible-joint robot closely resembles the magnitude of the velocity jump of the flexible-joint model with soft contact. Second, the flexible-joint model response oscillates around response of the rigid-robot model. To illustrate these facts on a specific simulation, the joint velocities for the representative impact scenario with an approach angle of 30 degrees with respect to the horizontal plane and an impact velocity of 0.1 m/s in the direction of motion visualized in Figure 2 are shown in Figure 3. Besides the aforementioned observations, simulations with different inertia matrices in the impact map (using M , $M + B_\theta$, or $M + B_\rho$ as values for M_θ in (16)) show that using $M_\theta = M + B_\theta$ indeed leads to the most accurate rigid-robot model. Comparing the different post-impact responses one observes that the magnitude of the velocity jump does not match the velocity jump of the flexible-joint model in case M or $M + B_\rho$ are used as values for M_θ , as shown in Figure 3, nor does the resulting post-impact response in these cases describe the response around which the flexible-joint model oscillates.

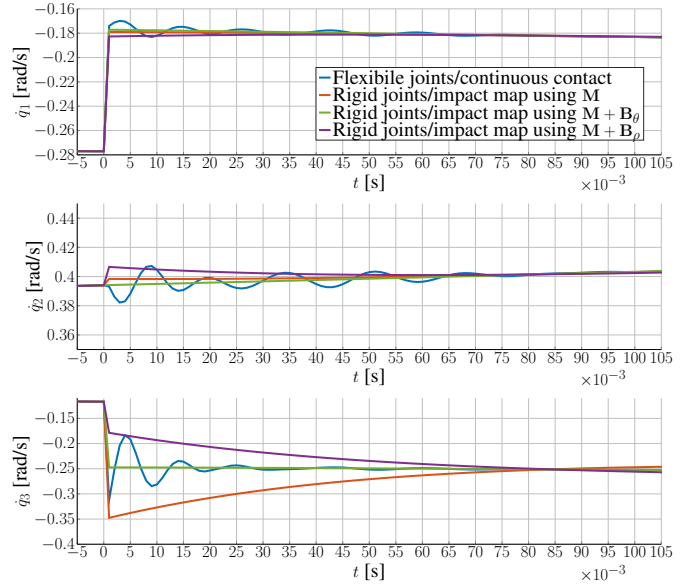


Fig. 3: Comparison of the post-impact joint velocities for a flexible-joint robot with a continuous contact model, and three instances of a rigid-joint robot with different inertia matrices used in the impact map for the impact scenario shown in Figure 2. The resulting velocities show that the reduced motor inertia matrix B_θ should be included in the impact map.

IV. EXPERIMENTAL VALIDATION

This section describes the experimental framework used to validate the introduced post-impact velocity predictor (16). Additionally, the results of the experiments are presented along with the respective analysis. These results are divided in two subsections, one where the focus of the analysis is set on the effect of the selected value of the modeled motor inertia, and another one where the action of the tangential friction term is examined.

A set of 50 experiments was recorded where a 7 DoF Franka Emika Panda robot with a spherical aluminum end-effector impacted a horizontal plate made of steel. During the recording process 10 different initial robot configurations along with the respective actuation joint torques required to impact the plate were set. For each of the 10 experiment types, 5 repetitions were run in order to prove the repeatability of the experiment type and little sensitivity of the prediction for very similar responses. These 10 groups of experiments can be subdivided in three main types depending on motion direction, each in turn subdivided according to different end-effector orientations. An overview of all types of experiments and additional details are given in Table II.

To command the robot for the experiments a virtual force is applied at the end effector. This virtual force is transformed to joint-torque commands via the end-effector Jacobian, which are sent to the robot via the Franka Control Interface (FCI) ⁶. The virtual force is applied for a fixed amount of time, and stopped before impact, causing the robot to move toward the

⁶Further details on <https://frankaemika.github.io/docs/overview.html>.

Experiment Type	Motion Direction	End-Effector Orientation
1	Forward (positive direction along x -axis)	-30° about y -axis
2		-20° about y -axis
3		-10° about y -axis
4		z -axis aligned with gravity
5	Backward (negative direction along x -axis)	30° about y -axis
6		20° about y -axis
7		10° about y -axis
8		z -axis aligned with gravity
9	Lateral (negative direction along y -axis)	-30° about x -axis
10		z -axis aligned with gravity

TABLE II: List of types of impact experiments. Each type is repeated five times. The motion direction and orientation indicate the end-effector impact modality.

steel plate while preventing interference of the controller on the post-impact response.

An offline impact detector was implemented for the automatic identification of the impact time in the recorded data. It detects sharp changes in q using the approximate joint acceleration, computed using *central differences*. First, a rough estimation of the impact time is determined automatically as the point where the approximate second derivative reaches its highest value within the entire set of samples of an experiment. Then, two intervals of ten samples are selected. An interval starts 15 samples before the time identified in the previous stage, to estimate the average value of the second derivative before impact. The other interval, centered at the rough estimation of the impact time, is used to look for the first instance where the value of the second derivative grows at least 8 times with respect to the average of the approximate ante-impact acceleration. The length of the interval and minimal growth rate were tuned by means of visual evaluation of the results over the 50 experiments. This approach searched joints 1 to 6 because it often retrieved false positives when applied to joint 7. The impact time was assumed to be the same for the seven robot joints.

During the experiments the robot starts from standstill and then accelerates due to the virtual force. After the virtual force is removed, the robot decelerates before it impacts the steel plate. This impact causes a jump in the velocity signal, after which the post-impact response shows oscillations. These oscillations damp out after about 100 ms, as shown in Figure 4. Afterwards, the arm continues to move until being stopped by its own joint friction. An experiment of type 1 (see Table II) is illustrated in Figure 4.

As in [1], we are mainly interested in predicting the gross velocity jump after an impact, discarding the impact-induced oscillations. Therefore, we need a procedure to filter out these oscillations. Differently from what is done in [1], a polynomial least squares fit is obtained from the post-impact joint position time-based signal, and the gross velocity at impact time is estimated by evaluating the derivative of the polynomial (in [1], the nonlinear fitting is performed on the velocity signal). The fitting is applied to samples over a span of 100 ms, starting at the impact time. We have found that a third order polynomial is sufficient in capturing the evolution of joint position trajectories. The interval length was selected as a result of the qualitative analysis of the velocity signals throughout the 50

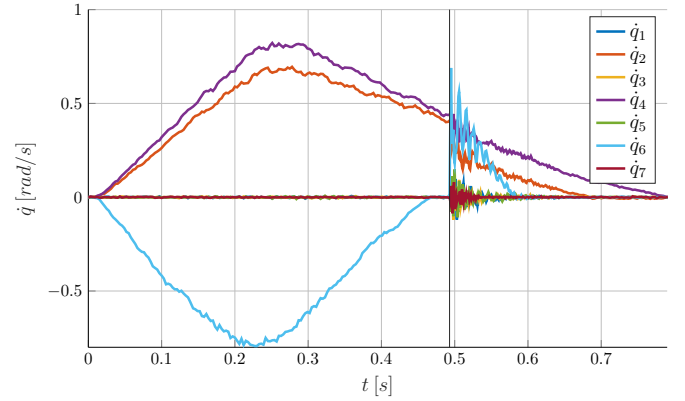


Fig. 4: Joint velocities during an impact experiment (type 1 in Table II). The vertical line denotes the impact time.

recorded experiments, that showed that 100 ms corresponds in all cases to the approximate duration of the oscillations present in the post-impact response of the robot (cf. oscillations in Figure 4). This approach turned out to be simpler and more robust than the nonlinear least-square approach proposed in [1], that can get stuck in local minima, providing essentially the same result when both methods converge.

The polynomial fit applied to the oscillatory post-impact response has good results, as illustrated by the representative post-impact response of joint 6 in Figure 5. This fit is used for assessment of the prediction accuracy as explained later in detail, since the oscillations provoked by the impact are disregarded by the predictor. However, note that the observed impact time in Figure 5 is not completely accurate, as the ante-impact velocity is initially zero and there is a significant growth to about 1 °/s when the impact is detected.

In regard to the impact time detection, this study also revealed that different joints exhibit a gradual lag in the time of impact, with the first joint showing signs of impact at a later instance, when compared to joint 6.

A. Selection of motor inertia constant

The numerical validation presented in Section III shows that using $\mathbf{M} + \mathbf{B}_\theta$ as the inertia matrix within the post-impact

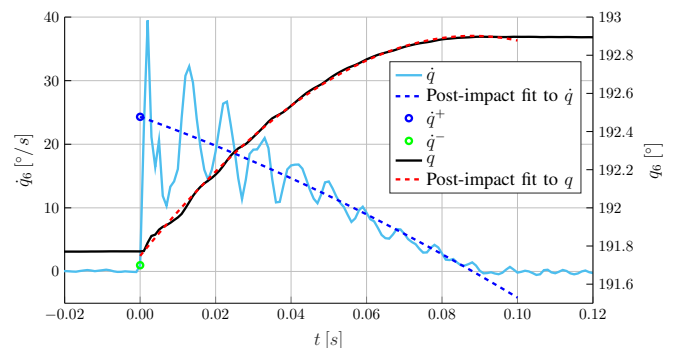


Fig. 5: Close-up of joint 6 velocity for the impact experiment displayed in Figure 4 (type 1 in Table II).

velocity predictor delivers the most accurate results. In the following we provide experimental evidence that this is indeed the case for joint 6 also by comparing it to the prediction obtained using \mathbf{B}_ρ as the modeled motor inertia, in place of \mathbf{B}_θ .

The results of the prediction over the whole set of 50 experiments were assessed based on the *quantitative comparison procedure* proposed in Section IV of [1] that enables a quantitative evaluation of the prediction by comparing the experimental post-impact data, containing oscillations, and the post-impact velocity estimated by the predictor derived using nonsmooth mechanics theory. The absolute error metric is selected in this study for the assessment,

$$e = |\hat{\mathbf{q}}_i^+ - \hat{\mathbf{q}}_i^+|, \quad (17)$$

where $\hat{\mathbf{q}}_i^+$ is the *virtual rigid-body post-impact velocity* for joint i obtained via the polynomial fitting procedure described previously, considered as the ground truth value, and $\hat{\mathbf{q}}_i^+$ is the *predicted rigid-robot post impact velocity* for joint i .

The influence of the selected dynamic model motor inertia on the prediction of the post-impact velocity was assessed graphically in a joint-wise fashion. Comparing the mean values obtained for the experiments of type 1 it became clear that the prediction based on \mathbf{B}_θ is more accurate overall than the prediction based on \mathbf{B}_ρ . This means that the predictions using \mathbf{B}_θ are in general closer to the post-impact velocity obtained via the polynomial fit, as illustrated by the representative results shown in Figure 6. In both predictions, surface friction at impact is accounted for. The effect of surface friction on the post-impact velocity prediction will be discussed later.

A comparison of the average absolute prediction error for \mathbf{B}_θ and \mathbf{B}_ρ , for each of the 10 types of experiments, shows that in many cases there is not a significant difference in the absolute prediction error, as illustrated by the values provided in Table III. There are some highlighted cells in the table, where the difference between the magnitudes of the absolute error in the predictions, for the two aforementioned motor

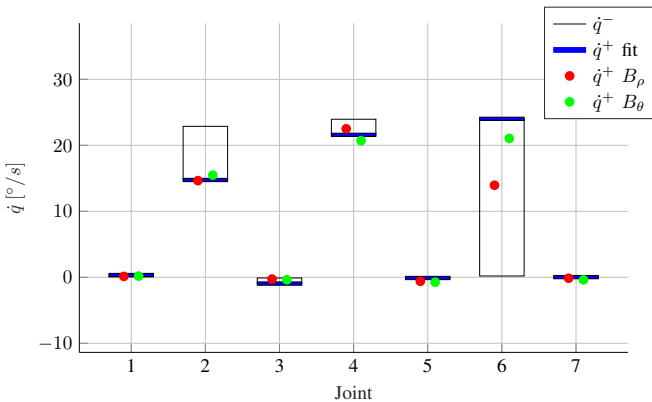


Fig. 6: Mean values of virtual rigid-body post-impact velocity (blue line), measured ante-impact velocity (black line), and predictions for each joint from 1 to 7 using different motor inertia constants, \mathbf{B}_θ (green) and \mathbf{B}_ρ (red) (over experiments of type 1 in Table II).

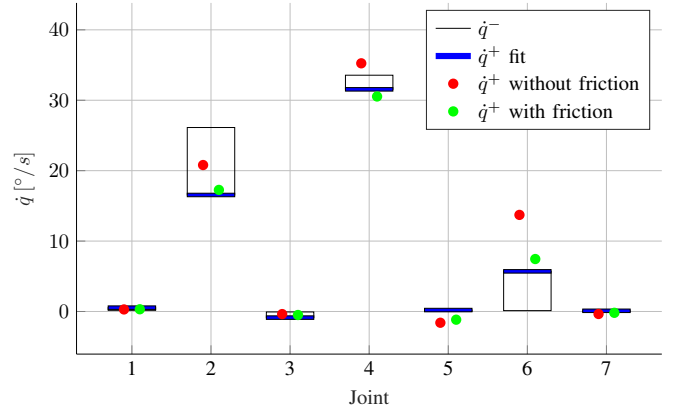


Fig. 7: Mean values of virtual rigid-body post-impact velocity (blue line), measured ante-impact velocity (black line), and predictions for each joint from 1 to 7 with (green) and without (red) considering tangential friction (over experiments of type 4 in Table II).

inertia matrices, goes over a threshold of 1.0 $^\circ/\text{s}$. This threshold is selected based on a qualitative analysis, of plots such as the one displayed in Figure 6, since this value indicates a significant difference when the scale of the y -axis (\dot{q}) is kept constant over the entire set of experiments. For error prediction differences above 1 $^\circ/\text{s}$, cases where the prediction with \mathbf{B}_θ is significantly better than the prediction with \mathbf{B}_ρ are highlighted in green, in the opposite case the cells are highlighted in red.

Although there is not a significant difference in the prediction accuracy overall, for joint 6 the inclusion of \mathbf{B}_θ in the predictor improves the accuracy considerably for most experiment types. In contrast, this choice of motor inertia seems to slightly worsen the prediction for joint 5 in some experiments favoring the use of \mathbf{B}_ρ (red color in Table III), but this is in general a smaller effect when compared with the gain in prediction accuracy that one gets in joint 6 that is the most affected by the impacts (cf. Figure 6).

B. Tangential Coulomb friction between the end-effector and the impacted surface

A value of 0.3 was identified for the friction coefficient between the spherical aluminum end-effector and the impacted steel plate. This parameter was tuned through the minimization of the prediction error for one of the experiments (type 4 in Table II) as a function of the selected friction coefficient included in $\tilde{\mathbf{J}}_\mu$ for the predictor expression (16). The friction coefficient retrieved by the optimization was the same using either of the two model motor inertia constants, i.e., either \mathbf{B}_θ or \mathbf{B}_ρ . Moreover, the identified magnitude of the friction coefficient was verified using a force gauge, that provided a similar value (difference below 10%).

In order to compare the accuracy of the prediction between the scenario where no friction is considered and the one with a tangential Coulomb component with $\mu = 0.3$, \mathbf{B}_θ is set as the motor inertia included in the predictor. The predictions including this friction component are much closer to the post-impact velocity obtained using the polynomial fit, as illustrated

Exp. Type #	Joint 1		Joint 2		Joint 3		Joint 4		Joint 5		Joint 6		Joint 7	
	\mathbf{B}_θ $\hat{\mathbf{q}}_i^+$	\mathbf{B}_ρ $(\hat{\mathbf{q}}_i^-)$												
1	0.17	0.21	0.73	0.46	0.57	0.68	0.88	0.91	0.64	0.50	2.97	10.06	0.42	0.17
	0.34	(0.08)	14.74	(22.87)	-0.96	(-0.10)	21.58	(23.95)	-0.11	(-0.03)	24.01	(0.19)	0.02	(-0.00)
2	0.16	0.18	0.23	0.57	0.28	0.37	0.41	1.32	0.55	0.41	6.62	12.67	0.48	0.25
	0.18	(0.04)	21.32	(27.42)	-0.56	(-0.01)	34.04	(36.34)	-0.08	(0.01)	24.53	(0.18)	0.05	(-0.08)
3	0.24	0.29	0.62	0.57	0.65	0.77	0.61	1.47	1.02	0.79	5.39	10.15	0.31	0.15
	0.39	(0.06)	20.44	(27.47)	-0.99	(-0.06)	35.54	(37.92)	0.26	(0.00)	17.90	(-0.02)	0.08	(0.03)
4	0.24	0.32	0.72	1.28	0.37	0.56	1.01	1.00	1.37	0.89	1.75	1.49	0.29	0.19
	0.54	(0.17)	16.55	(26.13)	-0.87	(-0.06)	31.55	(33.56)	0.20	(0.02)	5.70	(0.12)	0.10	(-0.01)
5	0.22	0.33	2.38	1.41	0.11	0.15	1.35	0.16	3.11	1.23	4.36	9.65	0.24	0.19
	0.50	(-0.02)	-8.93	(0.69)	-0.37	(-0.03)	-17.02	(-26.04)	-0.93	(-0.50)	-12.97	(0.31)	-0.21	(-0.08)
6	0.15	0.22	1.14	0.68	1.15	1.00	0.85	1.51	3.76	1.84	1.41	1.13	0.90	0.54
	0.29	(-0.07)	-8.29	(0.50)	0.86	(0.12)	-14.56	(-24.84)	0.21	(0.00)	1.68	(0.41)	-0.44	(-0.04)
7	0.10	0.21	1.09	0.88	1.06	0.89	0.35	0.21	3.22	1.64	0.86	2.89	1.18	0.63
	0.32	(0.00)	-7.57	(0.92)	0.72	(0.04)	-14.32	(-22.09)	0.25	(-0.04)	8.23	(0.08)	-0.45	(0.00)
8	0.29	0.36	0.49	0.20	0.53	0.38	1.13	0.80	1.47	0.31	5.90	11.63	0.96	0.29
	0.46	(0.02)	-6.70	(0.47)	0.15	(-0.08)	-13.92	(-21.65)	-0.74	(0.03)	20.35	(0.12)	-0.20	(-0.12)
9	0.30	0.28	2.16	2.15	1.52	1.44	0.93	1.02	4.32	2.21	1.83	2.35	0.06	0.07
	-8.31	(-9.60)	-2.52	(4.76)	-1.46	(-3.84)	-2.46	(-5.22)	0.12	(-0.01)	4.19	(0.05)	-0.08	(-0.14)
10	0.41	0.44	1.04	0.87	0.69	1.08	0.44	1.03	0.90	0.80	1.10	2.58	0.48	0.36
	-9.46	(-9.59)	-0.79	(4.39)	-2.64	(-5.28)	-2.86	(-4.64)	0.54	(0.01)	8.08	(0.04)	0.22	(-0.06)

TABLE III: Table of average absolute prediction error [$^\circ/\text{s}$] for comparison of \mathbf{B}_θ and \mathbf{B}_ρ . Cells highlighted in green show a significantly (at least $1.0^\circ/\text{s}$ difference) better performance of the predictor that uses \mathbf{B}_θ , when compared to the predictor that includes \mathbf{B}_ρ . Cells are highlighted in red in the opposite case. The use of \mathbf{B}_θ improves the accuracy of the prediction for joint 6, while the incorporation of \mathbf{B}_ρ results in an enhancement for joint 5. The virtual rigid-body post-impact velocity ($\hat{\mathbf{q}}_i^+$) and the ante-impact velocity ($\hat{\mathbf{q}}_i^-$) [$^\circ/\text{s}$] are displayed to describe the gross velocity jump induced by the contact.

Exp. Type #	Joint 1		Joint 2		Joint 3		Joint 4		Joint 5		Joint 6		Joint 7		
	<i>Friction coefficient</i>	0.3	0.0	0.3	0.0	0.3	0.0	0.3	0.0	0.3	0.0	0.3	0.0		
1		0.17	0.16	0.73	3.26	0.57	0.57	0.88	3.80	0.64	1.26	2.97	2.18	0.42	0.53
2		0.16	0.15	0.23	2.19	0.28	0.31	0.41	3.63	0.55	1.07	6.62	6.12	0.48	0.56
3		0.24	0.24	0.62	2.97	0.65	0.70	0.61	3.66	1.02	1.46	5.39	3.08	0.31	0.41
4		0.24	0.25	0.72	4.25	0.37	0.50	1.01	3.70	1.37	1.80	1.75	8.02	0.29	0.45
5		0.22	0.28	2.38	0.98	0.11	0.12	1.35	4.24	3.11	2.33	4.36	12.81	0.24	0.31
6		0.15	0.17	1.14	1.01	1.15	1.13	0.85	5.85	3.76	3.06	1.41	19.58	0.90	0.28
7		0.10	0.13	1.09	1.60	1.06	1.07	0.35	4.31	3.22	2.76	0.86	16.99	1.18	0.63
8		0.29	0.30	0.49	2.53	0.53	0.60	1.13	5.25	1.47	1.19	5.90	18.63	0.96	0.54
9		0.30	0.19	2.16	1.77	1.52	4.05	0.93	0.66	4.32	5.21	1.83	10.84	0.06	0.56
10		0.41	0.45	1.04	0.36	0.69	3.73	0.44	0.68	0.90	1.86	1.10	1.38	0.48	0.49

TABLE IV: Table of average absolute prediction error [$^\circ/\text{s}$] for analysis of the effects of the friction term on the predictor. Cells highlighted in green show a significantly (at least $1.0^\circ/\text{s}$ difference) better performance of the predictor that accounts for friction, when compared to the predictor that assumes frictionless impact. Cells are highlighted in red in the opposite case. The consideration of a tangential Coulomb friction term improves the accuracy of the prediction overall.

by the representative mean results of the experiments of type 4 in Figure 7. There the green dots representing the predictions with friction are closer to the post-impact fit, shown in blue, than the predictions without friction, shown in red.

A comparison of the average absolute prediction error with and without friction, for each of the 10 types of experiments, shows that the inclusion of the tangential Coulomb friction term significantly improves its accuracy, as illustrated by the values provided in Table IV. In this case cells highlighted in green show a significantly (at least $1.0^\circ/\text{s}$ difference) better performance of the predictor that accounts for friction, when compared to the predictor that assumes frictionless impact. The average absolute prediction error is computed according to (17).

V. CONCLUSION AND FUTURE WORK

A refined post-impact velocity predictor for torque-controlled flexible-joint robots has been presented. The proportional gain of the low-level torque control has been shown to have an important effect on the impact dynamics of the torque-controlled flexible-joint robots by means of numerical simulation and experimental validation. The inclusion of this effect in conjunction with the surface friction brings the absolute error of the post-impact velocity prediction down from tens of $^\circ/\text{s}$ to values below $7.0^\circ/\text{s}$ as shown in Tables III and IV. This error reduction is achieved with respect to the previously proposed method by the authors. An equivalent, but simpler and more robust virtual rigid-robot post-impact velocity estimate has also been introduced, based on polynomial fitting. Follow-up studies could explore methodologies to further improve the

accuracy of the offline impact time detector.

ACKNOWLEDGEMENTS

This work was partially supported by the Research Project I.A.M. through the European Union H2020 program under GA 871899.

REFERENCES

- [1] I. Aouaj, V. Padois, and A. Saccon, “Predicting the post-impact velocity of a robotic arm via rigid multibody models: An experimental study,” in *2021 IEEE International Conference on Robotics and Automation (ICRA)*, IEEE, 2021, pp. 2264–2271.
- [2] S. S. M. Salehian and A. Billard, “A dynamical-system-based approach for controlling robotic manipulators during noncontact/contact transitions,” *IEEE Robotics and Automation Letters*, vol. 3, no. 4, pp. 2738–2745, 2018.
- [3] A. Saccon, N. van de Wouw, and H. Nijmeijer, “Sensitivity analysis of hybrid systems with state jumps with application to trajectory tracking,” in *53rd IEEE Conference on Decision and Control*, IEEE, 2014, pp. 3065–3070.
- [4] M. Rijnen, A. Saccon, and H. Nijmeijer, “On optimal trajectory tracking for mechanical systems with unilateral constraints,” in *2015 54th IEEE Conference on Decision and Control (CDC)*, IEEE, 2015, pp. 2561–2566.
- [5] M. Rijnen, E. De Mooij, S. Traversaro, F. Nori, N. van de Wouw, A. Saccon, and H. Nijmeijer, “Control of humanoid robot motions with impacts: Numerical experiments with reference spreading control,” in *2017 IEEE International Conference on Robotics and Automation (ICRA)*, IEEE, 2017, pp. 4102–4107.
- [6] M. Rijnen, J. B. Biemond, N. van de Wouw, A. Saccon, and H. Nijmeijer, “Hybrid systems with state-triggered jumps: Sensitivity-based stability analysis with application to trajectory tracking,” *IEEE Transactions on Automatic Control*, vol. 65, no. 11, pp. 4568–4583, 2019.
- [7] J. J. van Steen, N. van de Wouw, and A. Saccon, “Robot control for simultaneous impact tasks via quadratic programming-based reference spreading,” in *2022 American Control Conference (ACC)*, IEEE, 2022, pp. 3865–3872.
- [8] Y. Wang, N. Dehio, and A. Kheddar, “On inverse inertia matrix and contact-force model for robotic manipulators at normal impacts,” *IEEE Robotics and Automation Letters*, vol. 7, no. 2, pp. 3648–3655, 2022.
- [9] Y. Wang, N. Dehio, and A. Kheddar, “Predicting impact-induced joint velocity jumps on kinematic-controlled manipulator,” *IEEE Robotics and Automation Letters*, vol. 7, no. 3, pp. 6226–6233, 2022.
- [10] J. Xie and N. Chakraborty, “Rigid body motion prediction with planar non-convex contact patch,” in *2019 International Conference on Robotics and Automation (ICRA)*, 2019, pp. 7646–7652.
- [11] J. Carpentier and P.-B. Wieber, “Recent progress in legged robots locomotion control,” *Current Robotics Reports*, vol. 2, no. 3, pp. 231–238, 2021.
- [12] Y. Hurmuzlu, F. Génot, and B. Brogliato, “Modeling, stability and control of biped robots—a general framework,” *Automatica*, vol. 40, no. 10, pp. 1647–1664, 2004, ISSN: 0005-1098.
- [13] S. Haddadin, A. De Luca, and A. Albu-Schäffer, “Robot collisions: A survey on detection, isolation, and identification,” *IEEE Transactions on Robotics*, vol. 33, no. 6, pp. 1292–1312, 2017.
- [14] J. Engelsberger, C. Ott, M. A. Roa, A. Albu-Schäffer, and G. Hirzinger, “Bipedal walking control based on capture point dynamics,” in *2011 IEEE/RSJ International Conference on Intelligent Robots and Systems*, 2011, pp. 4420–4427.
- [15] J. Engelsberger, C. Ott, and A. Albu-Schäffer, “Three-dimensional bipedal walking control based on divergent component of motion,” *IEEE Transactions on Robotics*, vol. 31, no. 2, pp. 355–368, 2015.
- [16] K. Bouyarmene and A. Kheddar, “Humanoid robot locomotion and manipulation step planning,” *Advanced Robotics*, vol. 26, no. 10, pp. 1099–1126, 2012.
- [17] S. Adly and N. N. Thieu, “Existence of solutions for a Lipschitzian vibroimpact problem with time-dependent constraints,” *Fixed Point Theory and Algorithms for Sciences and Engineering*, vol. 2022, no. 1, pp. 3–, 2022.
- [18] S.-S. Bi, X.-D. Zhou, and D. B. Marghitu, “Impact modelling and analysis of the compliant legged robots,” *Proceedings of the Institution of Mechanical Engineers, Part K: Journal of Multi-body Dynamics*, vol. 226, no. 2, pp. 85–94, 2012.
- [19] M. Jongeneel, C. A. Rey Arias, and S. Dingemans, *IAM archive containing impact experiments with a Franka Emika Panda robot*, 2023. DOI: 10.4121/21655631.V3.
- [20] W. Weekers and C. A. Rey Arias, *Refined post-impact velocity prediction for torque-controlled flexible joint robots*, <https://gitlab.tue.nl/robotics-lab-public/refined-post-impact-velocity-prediction>, 2023.
- [21] A. Albu-Schäffer, C. Ott, and G. Hirzinger, “A unified passivity-based control framework for position, torque and impedance control of flexible joint robots,” *International Journal of Robotics Research*, vol. 26, no. 1, pp. 23–39, Jan. 2007.
- [22] A. De Luca and W. J. Book, “Robots with flexible elements,” in *Springer Handbook of Robotics*, B. Siciliano and O. Khatib, Eds. Cham: Springer International Publishing, 2016, pp. 243–282.
- [23] A. S. Carvalho and J. M. Martins, “Exact restitution and generalizations for the hunt–crossley contact model,” *Mechanism and Machine Theory*, vol. 139, pp. 174–194, 2019.
- [24] K. H. Hunt and F. R. E. Crossley, “Coefficient of restitution interpreted as damping in vibroimpact,” *Journal of Applied Mechanics*, vol. 42, pp. 440–445, 2 1975.

- [25] C. Ott, “Cartesian impedance control of flexible joint manipulators,” Ph.D. dissertation, Universität des Saarlandes, 2005.
- [26] C. Gaz, M. Cognetti, A. Oliva, P. Robuffo Giordano, and A. De Luca, “Dynamic identification of the Franka Emika Panda robot with retrieval of feasible parameters using penalty-based optimization,” *IEEE Robotics and Automation Letters*, vol. 4, pp. 4147–4154, 4 2019.